DOI: 10.1002/cphc.201100981

Tailoring Broadband Antireflection on a Silicon Surface through Two-Step Silver-Assisted Chemical Etching

Chia-Yun Chen,* Wen-Jin Li, and Hsin-Hwa Chen[a]

In the past several decades, advances in nanofabrication have resulted in a great potential to improve both device performance and manufacturing process in various applications, such as electronics,[1–3] biochemical sensors,[4,5] and photovoltaic devices.[6,7] One revolutionary example is the incorporation of silicon nanostructures into the architecture of solar cells, enabling enhanced performance and cost-effective photovoltaic power generation because of their superior light trapping.[8–16] In particular, one-dimensional silicon (Si) nanostructures, including nanowires (NWs)[8–15] and nanopores (NPs),[16] are regarded as promising building blocks in the construction of radial p–n junctions in photovoltaic cells. These nanostructured designs facilitate the efficient collection of photogenerated carriers with low minority-carrier diffusion lengths,[17,18] and may benefit the relaxed requirement for Si quality and further enable the use of lower-cost solar cells.[10]

This striking property of Si NWs correlates with their unique light-trapping characteristics.[8–12] The increasing absorption of visible light in Si NWs is mainly attributed to the multiple scattering of incident waves when light passes through them. The inherent periodicity of NW arrays also responds to the excitation of guided resonances under illumination, significantly enhancing light absorption beyond the performance of bulk Si when a resonant condition occurs.[12] In addition, Si NWs with dimensions in the sub-wavelength scale posses broadband antireflection from the visible to the near-infrared regions.[13–15] Nevertheless, the resulting antireflection performance shows strong dependence on their structural geometry.[19] Nanostructures with tapered profiles dramatically suppress reflection loss over a large range of light wavelength because of its gradient refractive index between the air and the surface of the underlying substrate. In this aspect, the modification of the cylindrical morphology of Si NWs becomes a critical issue in further enhancing their antireflection performance.

Recently, researchers have found that the spectral reflection of taped Si NWs can be suppressed by shaping the tips of Si NWs via physical methods, such as high-density electron cyclotron resonance plasma etching[20] or reactive ion etching process.[21] Nevertheless, these approaches are unable to incorporate successive batches of texturization via wet chemical routes, in which the batch-type process of texturing Si surface benefits efficiently both the yield and the cost in the industrial standard of Si solar cells.[22,23] More critically, the involved disadvantages, such as high cost, complexities, and lengthy process, also inevitably impede their feasibility in industrial manufacturing. As a consequence, in the present work, textured nanostructures on Si surfaces were processed through an inexpensive, simple, and rapid two-steps wet-chemical etching to tailor their antireflection performances. Systematic investigations on distinct etching kinetics of polished and nanostructured Si surfaces were also conducted, respectively.

The process flow of two-step Ag-assisted chemical etching is shown in Figure 1a. In the first etching step, local oxidation and dissolution of Si atoms via galvanic displacement results in the formation of Ag nanoparticles with a surface density of the order of 10^{10} cm^{-2} (i). With the partial detachment and the dissolution of pre-deposited Ag nanoparticles in HNO_3 solution, the surface density of Ag nanoparticles significantly decreases to the order of 10^{8} cm^{-2} (ii). These Ag nanoparticles with wide separated distributions act as microscopic cathodes that initiate the formation of nanopore arrays (iii). The dissolution of Si atoms takes place beneath the Ag^{+}/Si interface, following this reaction [Eq. (1)]:[24]

$$Si + \frac{n}{2}H_2O_2 + 6HF \rightarrow nH_2O + H_2SiF_6 + \frac{4-n}{2}H_2 \quad (1)$$

After the etching process, the residual Ag nanoparticles are removed completely by a concentrated HNO_3 (65%) solution (iv). A top-view scanning electron microscope (SEM) image of the fabricated NP arrays is shown in Figure 1b. One can observe clearly the distinct nanopores with average sizes in the radial direction of 79 nm following the normal Gaussian distribution, as shown in the inset of Figure 1b. In addition, the surface fraction of Si is around 62%, as carefully estimated via SEM observations.

In the second etching step, dense aligned NW arrays are directly fabricated on the NP arrays (v), as illustrated in Figure 1a. The involved reaction can be represented as follows [Eq. (2)]:[25–27]

$$Si + 4Ag^{+} + 6HF \rightarrow H_2SiF_6 + 4Ag + 4H^{+} \quad (2)$$

Overall etching is initiated by the reduction of Ag ions on the Si surface because of the electrochemical potential of Ag^{+}/Ag, which is more positive than the Fermi level of Si. Accordingly, Ag seeds are formed on the top surface of NP arrays by injecting holes to the valence band of silicon. A preferential dissolution of Si at the Ag seed/Si interface is maintained by the reduction of more Ag ions, leaving the aligned NW arrays (vi). Subsequently, the concentrated HNO_3 solution is used

[a] Dr. C.-Y. Chen, Dr. W.-J. Li, Dr. H.-H. Chen
Material and Chemical Research Laboratories
Industrial Technology Research Institute
Rm. 834, Bldg. 52, 8F, 195, Sec. 4
Chung Hsing Rd., Chutung, Hsinchu (Taiwan)
Fax: (886) 3-5820207
E-mail: TimCYChen@itri.org.tw

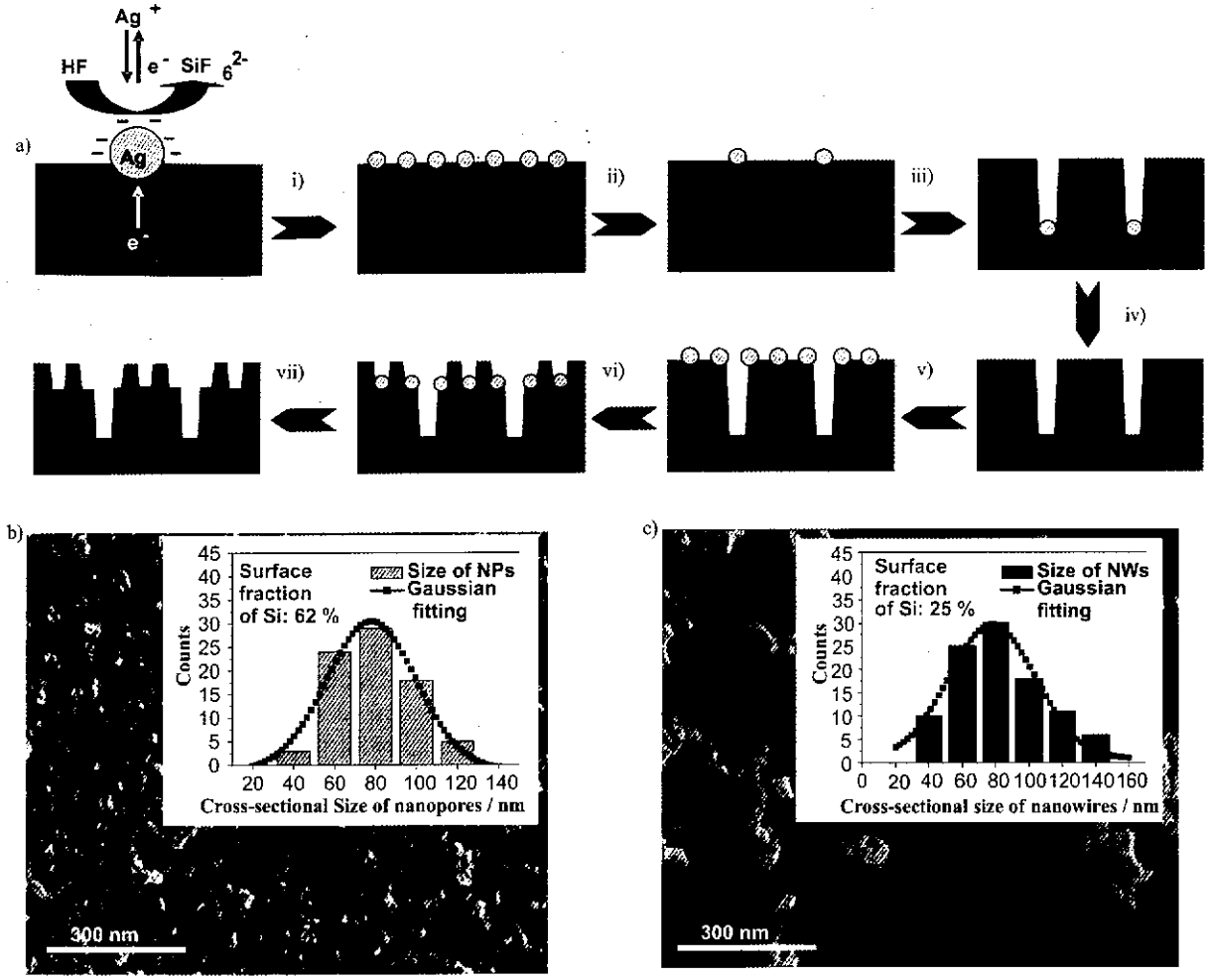

Figure 1. a) Schematic illustration of processes for preparing graded Si nanostructure arrays. b) Top-view SEM image of widely separated NP arrays. Inset: Size distribution of the as-prepared Si NPs. c) Top-view SEM image of dense NW arrays formed on the etched NP arrays. Inset: Size distribution of the as-prepared Si NWs.

again to dissolve the Ag nanoparticles covering the Si surfaces (vii). A top-view SEM image of the dense NW arrays fabricated on the etched NP arrays is shown in Figure 1c. There are no distinct differences in surface morphologies compared with the NW arrays formed on the published Si substrates.[25–27] The estimated distribution of NW diameters and fill factor are shown in the inset of Figure 1c, indicating normal Gaussian distributed diameters averaging 71 nm and 25% in the surface fraction of Si, respectively.

Figure 2a shows a cross-sectional view of combined nanostructure arrays. The top layer consists of dense NW arrays, followed by separated NP arrays directly in contact with the Si substrates, and which are referred to as graded nanostructure (GN) arrays. Both the NP and the NW arrays are formed along the <100> direction, which stands for the weakest back-bond strength of Si in crystallographic <100> orientation when the etching process occurs.[27,28] In contrast, an apparent interface exists between NW and NP arrays, owing to the difference in volume density of the Si component. In the formation of NP arrays, the straight sinking of Ag nanoparticles into the Si substrates is accomplished by local oxidation and etching beneath

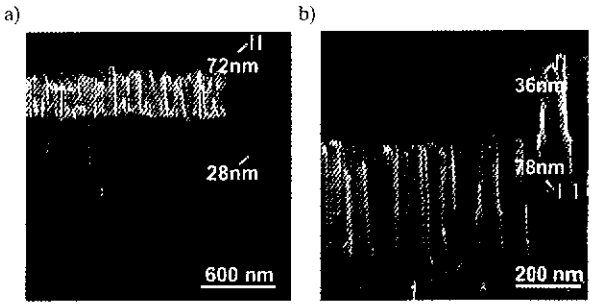

Figure 2. a) Cross-sectional SEM image of graded Si nanostructure arrays obtained by the two-step metal-assisted etching method. Inset: Representative SEM image showing the radius shrinkage of an NP along its axial direction. b) Cross-sectional SEM image of NW arrays formed on the etching NP arrays. Inset: Representative SEM image showing the dissimilar sizes of an NW at apex and root.

the Ag, resulting in separated NP arrays perpendicular to the substrates. Meanwhile, the Ag nanoparticles also experience a size reduction caused by the dissolution of H_2O_2/HF etchants, accounting for the cone-shaped morphology of the nanopores formed in the H_2O_2/HF etching electrolytes.[29]

As shown in the inset of Figure 2a, the radius of the pores along their axial direction gradually shrinks from 72 to 28 nm. Figure 2b presents a representative SEM image of NW arrays formed on the etching NP arrays. Noticeably, as denoted in the inset of Figure 2b, the diameters of the NWs, from apex to root, are not identical, which is different from previous results, where the NWs fabricated by catalytic etching were uniform in the axial direction.[14,25–29] The distributed diameters of the NW stem from the non-uniform etching rates of each Ag seed, implying that the wide distributions of Ag clusters are randomly nucleated when galvanic replacements start to take place on the Si surfaces.

To reveal the kinetics of catalytic etching on NP arrays, the lengths of the NW arrays directly etched on the NP arrays are first investigated under various etching times, from 1 to 2.8 min, respectively. For comparison, a similar etching process is also performed on the polished Si substrates. As shown in Figure 3a, the NW lengths demonstrate a linear dependence on etching time in both cases; whereas their etching rates, that is, the slopes of linear curves, are apparently different. The estimated etching rates are around 0.80 and 0.45 $\mu m\,min^{-1}$ for the catalytic etching on the polished substrates and on the NP arrays, respectively. Next, we intersected both time-dependent relations at time = 0 s and the corresponding intersection are 0 and −97 nm on polished substrates and NP arrays, respectively. With regard to the dissolution of Si, preferentially along the <100> orientation in the catalytic etching process, a competitive reaction must exist to influence the etching front of the NP arrays in the beginning of the etching process. Figure 3b illustrates the origin of the distinct etching kinetics on the polished and on the NP substrates. On the polished surface of Si, a directional etching of Si is accompanied with the reduction of Ag ions at the localized Ag^+/Si interface, which guarantees the vertical Si NWs afterward. On the NP substrates, however, the rough surfaces of NPs are more favorable for Ag nucleation because of the lower energy barrier for hole injection on defective sites. The effective nucleation of Ag correlates with the formation of Ag nuclei with wide and random distributions. In the electrochemistry aspect, the local current density in rough surfaces is well above the critical current density, J_{ps}, and, therefore, polishing of Si occurs.[24,30] The competitive process between polishing and directional etching on Si sustains until the defective sites of the Si surfaces are removed from the polishing process. Electrons from the structural defects of rough Si surfaces gradually become insufficient in providing effective nucleation of Ag. Subsequently, the directional etching of Si starts to dominate the etching phenomena, starting from time = 15 s, leaving the aligned NWs afterward (Figure 2b).

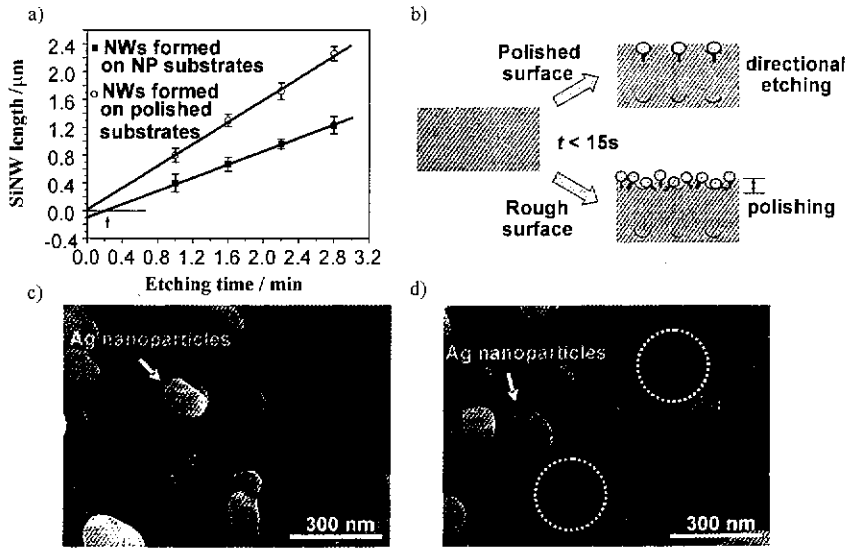

Figure 3. a) Linear relationship between etching time and length of the NWs formed on polished and NP substrates, respectively. The arrow denotes that the length of the NWs formed on the NP substrates starts to linearly depend on the etching time at 15 s. b) Visualization of the distinct etching mechanisms at polished and rough surfaces, respectively. The surface morphologies of the etched pores on c) polished substrates and d) NP arrays are demonstrated. The circles in (d) evidence the formation of small pits on the top surface of the NWs formed on the NP substrates.

To gain insights into the morphology of the etching front and interface, a short period of the etching process (time = 1 min) is performed on both the polished and the rough Si surfaces, in which the latter undergoes the formation of NPs in advance, as shown in Figures 3c,d. In addition to the similar characteristics of porous Si formation, a noticeable difference in the surface morphology between the polished and the NP substrates is the many small pits that remain on the top surface of the NP arrays (Figure 3d). This result clearly evidences that the dense nucleation and the spreading movement of the Ag nanoclusters causes Si polishing on the rough Si substrates at the initial stages. Nevertheless, no obvious pits are formed on the polished substrates, but solely vertical pores are formed due to the directional dissolution of Si, as shown in Figure 3c.

The optical properties of nanostructures possess significant dependence on their structural geometry. In GN arrays, there are two representative layers, the dense NWs, with $Si_{fraction}$ = 25%, and the separated NPs, with $Si_{fraction}$ = 62% on the surfaces, respectively. Unlike the individual NW or NP arrays used as antireflection layers, the GN arrays further allow flexibility to enhance their antireflection performances, which are extremely in demand in the high conversion efficiency of solar cells.[13,14] Figure 4a shows morphology evolutions of four various GN arrays, in which the overall thickness of the GN arrays are maintained at 1800 ± 75 nm by performing 40 s of the first etching step. Nevertheless, the thickness of the NW arrays is well modulated at 420 ± 70 nm (GN-I), 670 ± 60 nm (GN-II),

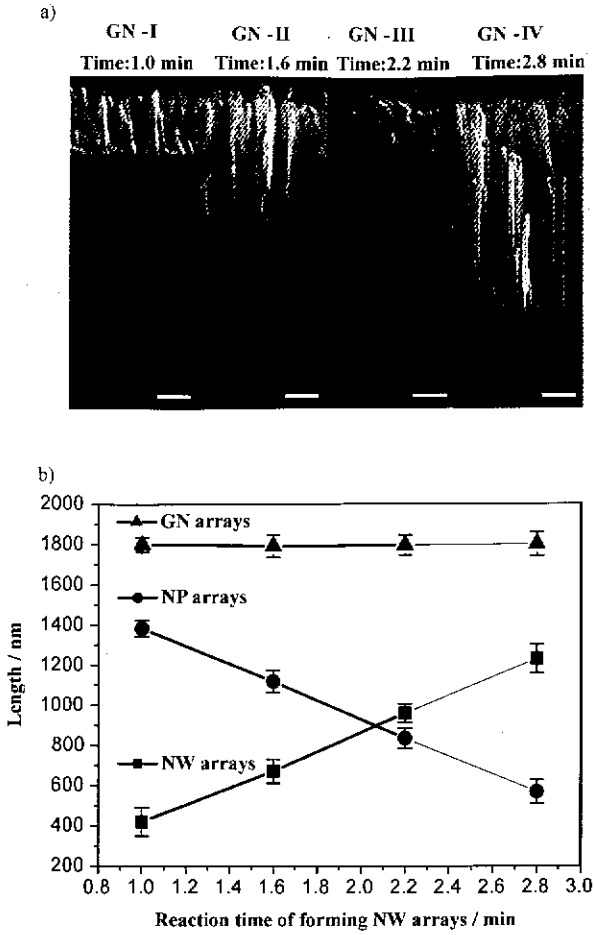

Figure 4. a) Morphology evolutions of four different GN arrays. The total thickness of each GN array is maintained at (1800±75) nm. The scale bar is 200 nm. b) Plot of reaction time of forming NW arrays versus length of various GN arrays, with a combination of NP and NW arrays.

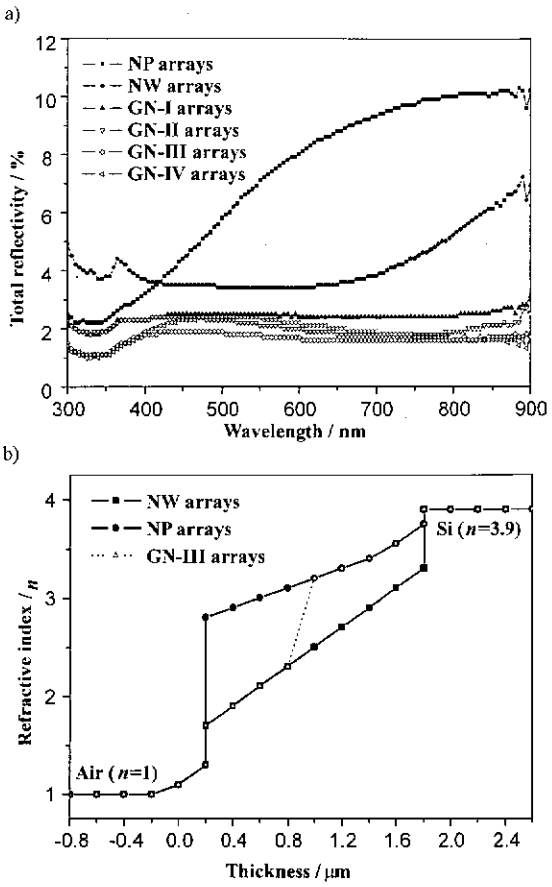

Figure 5. a) Optical reflectance spectra of NP, NW and various GN arrays. b) Effective refraction index of NP, NW and GN–III arrays calculated by the weighting formula.

960±45 nm (GN-III), and 1230±70 nm (GN-IV) by tuning the etching durations of the second etching step, followed by a linear characteristic of the NW length on the etching time, as shown in Figure 4b. Notice that all the four GN arrays present smooth composite interfaces between the NP and the NW arrays, and that these features—along with the adjustable profiles of the combined nanostructures—provide a simple and reproducible method for tailoring antireflection properties.

The total reflectance spectra of the four distinct GN arrays are shown in Figure 5a. For comparison, similar measurements are also performed on individual NW and NP arrays with the same thickness as that of GN arrays (1800±80 nm). As shown in Figure 5a, all the structures manifest suppressed reflectivity compared to polished Si (>35%).[31] The sub-wavelength feature of the nanostructures leads to multiple scattering of sunlight across them to greatly enhance their capability of light trapping. More importantly, compared to the individual NW or NP arrays, all the GN arrays reduce the reflectance between the air and the Si substrates over the major spectral irradiance of sunlight more effectively. These combined nanostructures essentially introduce the gradient refraction index at each interface in which the high density of vertical pores at the upper layer of the GN arrays can dramatically reduce the mismatch in refraction index at the air/$GN_{upper\ layer}$ interface. On the other hand, the steady transition of morphology at $GN_{lower\ layer}$/Si is fulfilled by the low density of vertical pores in the lower layer of the GN arrays. Leading among those four distinct GN layers is GN–III, whose average reflectivity is suppressed to 1.6%, approximately 39% less than single NP arrays and 20% less than individual NW arrays, as summarized in Table 1. To elucidate their suppressed reflection, the profile of effective refraction index, $n_{eff}(\lambda)$, at 600 nm in different antireflection morphologies is determined by the following weighting formula [Eq. (3)]:[32]

$$n_{eff}(\lambda) = f \times n_{Si}(\lambda) + (1 - f) \times n_{Air}(\lambda) \quad (3)$$

where f is the fraction of Si, and $n_{Si}(\lambda)$ and $n_{Air}(\lambda)$ correspond to the refraction indices of Si and air at 600 nm, respectively. The

Table 1. Average reflectivity (300–900 nm) of various nanostructure arrays.

NP arrays	NW arrays	GN–I arrays	GN–II arrays	GN–III arrays	GN–IV arrays
7.1%	4.2%	2.4%	2.1%	1.6%	1.8%

calculated effective n ($\lambda = 600$ nm) values of the NP, NW, and GN–III arrays are plotted in Figure 5b. In the NW arrays, the effective n gradually changes across the air/NW_{apex} interface, but sharply changes across the NW_{root}/Si substrates (from $n = 3.3$ to $n = 3.9$), resulting in higher surface reflection in the latter. On the contrary, in the NP arrays with separated vertical pores, the effective n sharply changes from 1 to 2.8 at air/NP_{apex}, and then steadily changes from 3.7 to 3.9 across the NP_{root}/Si substrates. The overall reflectivity is still suppressed, but is slightly larger than the NW arrays, as shown in Table 1. In the GN–III arrays with dense NWs along with separated NP arrays, the effective n at both interfaces changes smoothly, leading to lower light reflection beyond single NW or NP arrays.

In addition, the correlation of optical reflectivity with respect to the thickness of the antireflection layers is further investigated. As shown in Figure 6, the different lengths of NW and GN-III arrays are prepared to evaluate their antireflection performances. Evidently, in both cases, the corresponding reflectivity is gradually decreased by the longer length of the nanostructures, respectively. These trends are consistent with previous studies.[33] In particular, the GN–III arrays demonstrate a sharper decrease in reflectivity than the NW arrays at 400, 600, and 800 nm of light irradiance, showing better antireflection performance over the major spectral irradiance of sunlight.

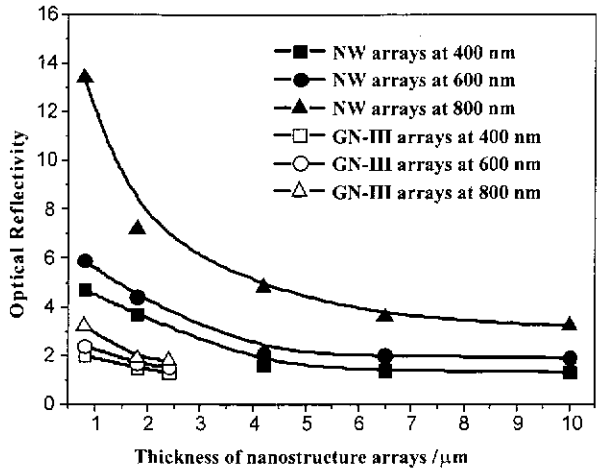

Figure 6. Optical reflectivity (at 400, 600 and 800 nm) of individual NW arrays and GN–III arrays with various thicknesses.

In summary, we have developed combined nanostructure arrays with tailored structural profiles. Systematic investigations of the distinct etching kinetics of the Si morphologies indicate that Si polishing is predominant on the NP arrays until catalytic etching is sustained for 15 s. Then, directional etching becomes more effective. Thus, aligned Si NW arrays are subsequently formed, with a linear dependence of the NW length on the etching time. By simply controlling the etching time, various GN arrays can be fabricated, with smooth composite interfaces between the NP and NW arrays and adjustable profiles. These tailored nanostructures possess a sharper decrease in reflectivity over the major irradiance of sunlight because of their smooth change in effective refraction index between the air and beneath the Si, further promising a low-cost, large-area, and versatile technique in diverse applications, including optical and electro-optical devices and other antireflection designs.

Experimental Section

Two-step Ag-assisted chemical etching was performed on single-crystal p-doped Si wafers with a resistivity of 0.01–0.05 Ωcm. Prior to the etching process, the Si substrates were cleaned by sequentially rinsing them with acetone, ethanol and deionized water several times. In the first etching step, the clean substrates were soaked in an aqueous solution containing 0.02 M $AgNO_3$ and 4.5 M HF at 25 °C for 30 s. After rinsing, the substrates were then soaked in a diluted HNO_3 (6%) solution for 10 min. Finally, the samples were soaked in an aqueous solution of 0.3 M H_2O_2 and 4.5 M HF at 50 °C for 40 s to form separated NP arrays. The involved reactions are as follows [Eqs. (4) and (5)]:[24,28,29]

Cathodic reaction :

$$H_2O_2 + 2H^+ \rightarrow 2H_2O - 2h^+ \quad E^0 = +1.76\,V \tag{4}$$

Anodic reaction :

$$Si + 6F^- \rightarrow SiF_6^{2-} + 4e^- \quad E^0 = -1.24\,V \tag{5}$$

The residual Ag nanoparticles were removed completely by dipping the substrates in a concentrated HNO_3 (65%) solution. A top-view SEM image of the fabricated NP arrays is shown in Figure 1b. In the second etching step, a mixture of 0.02 M $AgNO_3$ and 4.5 M HF at 50 °C for 1 min was used to construct dense aligned NW arrays. The involved reactions are as follows [Eqs. (6) and (7)]:[25–28]

Cathodic reaction :

$$Ag^+ + e^- \rightarrow Ag \quad E^0 = +0.79\,V \tag{6}$$

Anodic reaction :

$$Si + 6F^- \rightarrow SiF_6^{2-} + 4e^- \quad E^0 = -1.24\,V \tag{7}$$

After that, a concentrated HNO_3 (65%) solution was used to remove the residual Ag nanoparticles. Stirring was not applied in any of our fabrication steps. A top-view SEM image of the fabricated NW arrays is shown in Figure 1c. The cross-sectional SEM image of graded Si nanostructure arrays obtained from the above two steps of metal-assisted etching is shown in Figure 2a. To reveal the kinetics of catalytic etching on NP arrays, 40 s of the first-step etching and various etching times (1, 1.6, 2.2 and 2.8 min) of the second-step etching were performed to fabricate NP and NW arrays, respectively, as shown in Figure 3a. To compare the antireflection performances, the single NP arrays were fabricated by performing the first-step etching for 40 s on the polished Si substrates, and the individual NW arrays were fabricated by performing the second-step etching for 2.5 min on the polished Si wafers, as shown in Figure 5a.

The morphologies of fabricated nanostructures were observed by SEM (JSM-6390).The total reflectance spectra of the four distinct GN arrays are measured using a UV/Vis spectrophotometer (U-3010, Hitachi) with an integrating sphere, in the wavelength of 300 to 900 nm.

Acknowledgements

The authors thank the Ministry of Economic Affairs (No. A301ARY461), Taiwan, for financially supporting this study.

Keywords: antireflection · chemical etching · nanostructures · refraction index · silicon

[1] E. Stern, J. F. Klemic, D. A. Routenberg, P. N. Wyrembak, D. B. T. Evans, A. D. Hamilton, D. A. LaVan, T. M. Fahmy, M. A. Reed, *Nature* **2007**, *445*, 519–522.
[2] Y. Cui, Z. Zhong, D. Wang, W. U. Wang, C. M. Lieber, *Nano Lett.* **2003**, *3*, 149–152.
[3] Y. Li, F. Qian, J. Xiang, C. M. Lieber, *Mat. Today* **2006**, *9*, 18–27.
[4] F. Patolsky, B. P. Timko, G. Yu, Y. Fang, A. B. Greytak, G. Zheng, C. M. Lieber, *Science* **2006**, *313*, 1100–1104.
[5] Y. Cui, Q. Wei, H. Park, C. M. Lieber, *Science* **2001**, *293*, 1289–1292.
[6] B. Tian, X. Zheng, T. J. Kempa, Y. Fang, N. Yu, G. Yu, J. Huang, C. M. Lieber, *Nature* **2007**, *449*, 885–890.
[7] Y. Dong, B. Tian, T. J. Kempa, C. M. Lieber, *Nano Lett.* **2009**, *9*, 2183–2187.
[8] L. Tsakalakos, J. Balch, J. Fronheiser, M. Y. Shih, S. F. LeBoeuf, M. Pietrzykowski, P. J. Codella, B. A. Korevaar, O. Sulima, J. Rand, A. Davuluru, U. Rapol, *J. Nanophotonics* **2007**, *1*, 013552.
[9] L. Hu, G. Chen, *Nano Lett.* **2007**, *7*, 3249–3252.
[10] E. Garnett, P. Yang, *Nano Lett.* **2010**, *10*, 1082–1087.
[11] J. Li, H. Y. Yu, S. M. Wong, X. Li, G. Zhang, P. G. Q. Lo, D. L. Kwong, *Appl. Phys. Lett.* **2009**, *95*, 243113.
[12] C. Lin, M. L. Povinelli, *Opt. Express* **2009**, *17*, 19371–19381.
[13] K. Peng, Y. Xu, Y. Wu, Y. Yan, S. T. Lee, J. Zhu, *Small* **2005**, *1*, 1062–1067.
[14] V. Sivakov, G. Andra, A. Gawlik, A. Berger, J. Plentz, F. Falk, S. H. Christiansen, *Nano Lett.* **2009**, *9*, 1549–1554.
[15] C. Chen, R. Jia, H. Yue, H. Li, X. Liu, D. Wu, W. Ding, T. Ye, S. Kasai, H. Tamotsu, J. Chu, S. Wang, *J. Appl. Phys.* **2010**, *108*, 094318.
[16] a) L. L. Ma, Y. C. Zhou, N. Jiang, X. Lu, J. Shao, W. Lu, J. Ge, X. M. Ding, X. Y. Hou, *Appl. Phys. Lett.* **2006**, *88*, 171907; b) K. Q. Peng, X. Wang, L. Li, X. L. Wu, S. T. Lee, *J. Am. Chem. Soc.* **2010**, *132*, 6872–6873; c) S. E. Han, G. Chen, *Nano Lett.* **2010**, *10*, 1012–1015.
[17] B. M. Kayes, H. A. Atwater, N. S. Lewis, *J. Appl. Phys.* **2005**, *97*, 114302.
[18] S. M. Wong, H. Y. Yu, J. S. Li, Y. L. Li, N. Singh, P. G. Q. Lo, D. L. Kwong, *IEEE Electron Device Lett.* **2011**, *32*, 176–178.
[19] a) W. H. Southwell, *Opt. Lett.* **1983**, *8*, 584–586; b) C. C. Striemer, P. M. Fauchet, *Appl. Phys. Lett.* **2002**, *81*, 2980–2982; c) S. A. Boden, D. M. Bagn, *Appl. Phys. Lett.* **2008**, *93*, 133108; d) H. M. Branz, V. E. Yost, S. Ward, K. M. Jones, B. To, P. Stradins, *Appl. Phys. Lett.* **2009**, *94*, 231121; e) Y. Li, J. Zhang, S. Zhu, H. Dong, F. Jia, Z. Wang, Y. Tang, L. Zhang, S. Zhang, B. Yang, *Langmuir* **2010**, *26*, 9842–9847.
[20] Y. F. Huang, S. Chattopadhyay, Y. J. Jen, C. Y. Peng, T. A. Liu, Y. K. Hsu, C. L. Pan, H. C. Lo, C. H. Hsu, Y. H. Chang, C. S. Lee, K. H. Chen, L. C. Chen, *Nat. Nanotechnol.* **2007**, *2*, 770–774.
[21] Y. Li, J. Zhang, S. Zhu, H. Dong, Z. Wang, Z. Sun, J. Guo, B. Yang, *J. Mater. Chem.* **2009**, *19*, 1806–1810.
[22] P. Panek, M. Lipinski, J. Dutkiewicz, *J. Mater. Sci.* **2005**, *40*, 1459–1463.
[23] U. Gangopadhyay, S. K. Dhungel, P. K. Basu, S. K. Dutta, H. Saha, J. Yi, *Sol. Energy Mater. Sol. Cells* **2007**, *91*, 285–289.
[24] C. Chartier, S. Bastide, C. L. Clement, *Electrochim. Acta* **2008**, *53*, 5509–5516.
[25] K. Q. Peng, Y. J. Yan, S. P. Gao, J. Zhu, *Adv. Mater.* **2002**, *14*, 1164–1167.
[26] K. Q. Peng, H. Fang, J. J. Hu, Y. Wu, J. Zhu, Y. J. Yan, S. T. Lee, *Chem. Eur. J.* **2006**, *12*, 7942–7947.
[27] C. Y. Chen, C. S. Wu, C. J. Chou, T. J. Yen, *Adv. Mater.* **2008**, *20*, 3811–3815.
[28] Z. Huang, N. Geyer, P. Werner, J. Boor, U. Gosele, *Adv. Mater.* **2011**, *23*, 285–308.
[29] X. Zhong, Y. Qu, Y. C. Lin, L. Liao, X. Duan, *Appl. Mater. Interfaces* **2011**, *3*, 261–270.
[30] M. L. Chourou, K. Fukami, T. Sakka, S. Virtanen, Y. H. Ogata, *Electrochim. Acta* **2010**, *55*, 903–912.
[31] P. K. Singh, R. Kumar, M. Lal, S. N. Singh, B. K. Das, *Sol. Energy Mater. Sol. Cells* **2001**, *70*, 103–113.
[32] a) D. G. Stavenga, S. Foletti, G. Palasantzas, K. Arikawa, *Proc. R. Soc. B* **2006**, *273*, 661–667; b) H. C. Chang, K. Y. Lai, Y. A. Dai, H. H. Wang, C. A. Lin, J. H. He, *Energy Environ. Sci.* **2011**, *4*, 2863–2869.
[33] S. K. Srivastava, D. Kumar, P. K. Singh, M. Kar, V. Kumar, M. Husain, *Sol. Energy Mater. Sol. Cells* **2010**, *94*, 1506–1511.

Received: December 8, 2011
Revised: February 13, 2012
Published online on March 7, 2012

